

Full-Time, Eye-Safe Cloud and Aerosol Lidar Observation at Atmospheric Radiation Measurement Program Sites: Instruments and Data Processing

JAMES R. CAMPBELL AND DENNIS L. HLAVKA

Science Systems and Applications, Inc., Lanham, Maryland

ELLSWORTH J. WELTON

University of Maryland, Baltimore County, Baltimore, Maryland

CONNOR J. FLYNN AND DAVID D. TURNER

Pacific Northwest National Laboratory, Richland, Washington

JAMES D. SPINHIRNE AND V. STANLEY SCOTT III

NASA Goddard Space Flight Center, Mesoscale Atmospheric Processes Branch, Greenbelt, Maryland

I. H. HWANG

Science and Engineering Services, Inc., Burtonsville, Maryland

(Manuscript received 30 April 2001, in final form 28 September 2001)

ABSTRACT

Atmospheric radiative forcing, surface radiation budget, and top-of-the-atmosphere radiance interpretation involve knowledge of the vertical height structure of overlying cloud and aerosol layers. During the last decade, the U.S. Department of Energy, through the Atmospheric Radiation Measurement (ARM) program, has constructed four long-term atmospheric observing sites in strategic climate regimes (north-central Oklahoma; Barrow, Alaska; and Nauru and Manus Islands in the tropical western Pacific). Micropulse lidar (MPL) systems provide continuous, autonomous observation of nearly all significant atmospheric clouds and aerosols at each of the central ARM facilities. These systems are compact, and transmitted pulses are eye safe. Eye safety is achieved by expanding relatively low-powered outgoing pulse energy through a shared, coaxial transmit/receive telescope. ARM MPL system specifications and specific unit optical designs are discussed. Data normalization and calibration techniques are presented. These techniques, in tandem, represent an operational value-added processing package used to produce normalized data products for ARM cloud and aerosol research.

1. Introduction

The success, or failure, of global numerical climate simulations can be traced directly to the accuracy of the empirical relationships and input parameters required to replicate significant dynamic and radiative processes. Knowledge of the vertical structure of cloud and aerosol scattering properties or layers from varying climate regimes is fundamental. Analysis of surface or top-of-the-atmosphere radiative fluxes is not sufficient in itself. Models that can correctly define these fluxes may have erroneous heating and cooling rates embedded within the atmosphere. There are numerous variables and mea-

surements required to fully understand the radiative impact of cloud and aerosols, but accurate measurements of occurrence, height, and thickness are relatively sparse. Deficiencies in essential global observations combined with increasing anxiety surrounding the impact of fossil fuel consumption and various other human activities on the atmosphere are the focus of a great deal of ongoing research (e.g., Wielicki et al. 1995).

The Atmospheric Radiation Measurement (ARM) program marks one of the key components of the strategy of the U.S. Department of Energy to address cloud and aerosol research. The ARM philosophy (Stokes and Schwartz 1994) is to gather time-extended measurements from several locales by creating and operating long-term observing sites equipped with diverse arrays of passive and active remote sensing, as well as in situ instrumentation. Four such sites have so far been es-

Corresponding author address: James R. Campbell, c/o Code 912, NASA Goddard Space Flight Center, Greenbelt, MD 20708.
E-mail: campbell@virl.gsfc.nasa.gov

TABLE 1. A historical listing of all ARM MPL systems by site, including their dates of operation, optical configuration versions, and spatial (ΔV) and temporal (ΔT) data-acquisition resolution settings.

Site	Unit	Version	Dates	ΔV	ΔT
SGP	00	1.0	Dec 1993–Mar 1996	300 m	60 s
	02	1.0	Jan 1996–Aug 1998	300 m	60 s
	54	2.0	Sep–Nov 1998	30 m	30 s
TWP-M	03	1.0	Jan 1999–present	300 m	60 s
			Feb–Nov 1997		
			Apr 1998–Oct 1999		
TWP-N	59	1.0	Aug 1999–Apr 2001	30 m	30 s
			Dec 2001–present		
			Nov 1998–Jan 1999		
NSA	58	1.0	Apr 1999–Feb 2000	30 m	30 s
			Oct–Dec 2000		
			Apr 2001–present		
			Mar 1998–present		

tablished, representing three distinct regions: the mid-latitude continental [north-central Oklahoma (SGP)], tropical [Manus and Nauru Islands (TWP-M and TWP-N, respectively)], and polar [Barrow, Alaska (NSA)] regimes.

The direct detection of atmospheric cloud and aerosol generally involves active-based remote sensing techniques, such as radar and lidar. Lidar systems are particularly sensitive to smaller atmospheric particles due to their enhanced scattering at visible wavelengths (Sassen 1995). However, continuously running lidars (necessary for the full-time requirements of climate measurements) are a fairly recent development and represent a significant departure from traditional application. Costs combined with a maintenance-intensive nature have historically limited widespread lidar usage (Sassen 1991). Limited lifetimes and safety considerations arising from high-energy output are additional drawbacks. The micropulse lidar (MPL), developed in 1992 at the National Aeronautics and Space Administration (NASA) Goddard Space Flight Center (GSFC) (Spinhirne 1993) overcomes many such obstacles. MPL instruments are a long-standing member of the ARM instrument suite. The MPL technology applies advances in solid-state, diode-pumped lasers with appreciable operational lifetimes, and the introduction of high-efficiency quantum noise-limited photon counting devices. The most notable MPL feature is that its transmitted energy pulses are eye safe. Low pulse energies (microjoules—standard lidars are routinely orders of magnitude higher) are expanded through a shared Cassegrain transmitter/receiver (transceiver) telescope at a high repetition rate (2500 Hz). This eliminates the common safety requirement of supervised instrument operation, allowing them to be run autonomously.

ARM MPL data are processed for standard products, including the heights of cloud layers and the vertical distribution of optical scattering cross sections. Processed datasets and results are disseminated to the atmospheric research community through the ARM program. For users of MPL data a reference for instrument function, calibration, and data-retrieval methods is nec-

essary. In this paper we describe the MPL instruments and their use at ARM sites. We further describe the nature of measured raw signal and its normalization process. Analysis of error propagation and correction uncertainties in MPL processed signal can be found in a separate article by Welton and Campbell (2002, manuscript submitted to *J. Atmos. Oceanic Technol.*, hereafter WC02).

2. Instrument

MPL instruments detect nearly all significant tropospheric cloud and aerosol, to the limit of signal attenuation, through appreciable pulse summation and geometric signal compression (Spinhirne et al. 1995). Additionally, a narrow receiver field of view (approximately $100 \mu\text{rad}$) eliminates complications from multiple scattering and limits the effects of ambient solar background. The MPL package is rugged and compact, allowing for simple deployment and operation (given a stable, weatherproof environment). Systems have been demonstrated to run continuously for a period on the order of one year before requiring major maintenance. Aside from basic measurements of cloud boundaries, MPL data can be used to calculate cloud scattering cross sections and optical thicknesses, planetary boundary layer heights and aerosol extinction and optical thickness profiles, including those into the stratosphere in nighttime cases (Spinhirne 1993; Welton et al. 2001).

Table 1 notes the dates of operation, relevant diagnostic capabilities and settings for the historical and current ARM MPL units. Measurements at SGP began in December 1993, TWP-M in February 1997, NSA in March 1998, and TWP-N in November 1998. Specific revisions have been made to the MPL breadboard design described by Spinhirne (1993), as units began commercial production and distribution through Science and Engineering Systems, Inc. (SESI) of Burtonsville, Maryland. Over 20 MPL systems have since been produced. Accounting for optical upgrades and improved data-acquisition rates, four different versions of the

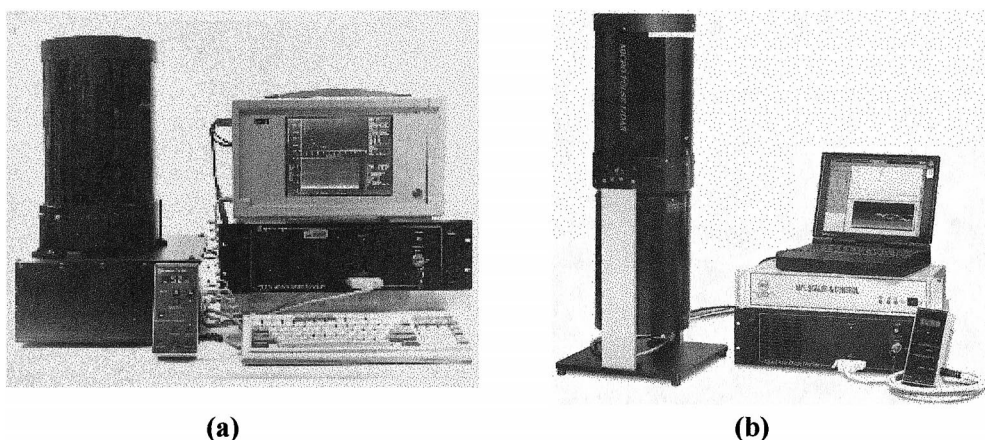


FIG. 1. MPL instrument casing versions alongside the multichannel scalar, laser power supply, and system laptop computer. (a) The prototype design (V1.0); (b) the upgraded canister design (V2.0).

MPL have been used among the seven historical ARM systems noted in Table 1.

ARM sites house large numbers of instruments, and they are typically remote in nature (raising the issue of timely maintenance initiative). Instrument simplicity and practicality therefore become valuable assets. Both of these characteristics figure prominently in the design of the MPL. Eye safety permits autonomous system operation without concern for user or bystander safety. It also indirectly contributes to a manageable package size. The singular transceiver design, required to expand outgoing pulse energies to make the beam eye safe, allows for a much smaller system compared to the more commonly used separate transmit/receive lidar optical design. Displayed in Figs. 1a and 1b are two versions of the MPL housing, respectively, alongside a multichannel scalar unit, laser power supply, and operating computer. The configuration in Fig. 1a (henceforth referred to as V1.0) was used through the first four ARM units (00, 02, 03, and 54). A schematic drawing of V1.0 can be found in Spinhirne et al. (1995). The base container (approximately $40 \times 40 \times 20 \text{ cm}^3$) houses all optical components, which are mounted mostly along the inside of its top panel. The transceiver is fastened atop the outside of this upper plate, with external cable connections accommodated along a backside plate. While particularly stable, V1.0 proved somewhat bulky and lacked a simple means for operating at nonzenith viewing angles. These concerns were addressed in the upgraded tubular casing design shown in Fig. 1b (V2.0), which is the model used for the more recently deployed ARM instruments (units 58, 59, and 72). The base optics box is replaced by two mounting plates: a 30-cm-long piece affixed slightly off of the 22-cm-diameter axis of the telescope bottom extending out behind it and a circular base plate attached perpendicular to the former at its end. The connected segment is covered with an aluminum cylinder. Optical components are fastened along the extension plate, while external interfaces are handled

along the back face. Pivoting rings fix the unit within two stanchions and a foundation plate allowing the transceiver to pivot over variable viewing angles, manually adjustable as desired. A tightening screw within the pivots adjusts the rigidity of the mount, thus fastening the unit in place to a desired viewing angle. Calibration of the system is made easier by simple manipulation of this angle (to be discussed). Total package volume for both system versions total well below 1 m^3 .

The MPL lasers are the diode-pumped Spectra Physics 7300-L3 Nd:YLF model, with 7960-L3 short cavity head (1047 nm, 1.0 W) and 7965-L3 frequency doubler module (523 nm). The diode rests in the laser power supply container, and is fiber-coupled externally to the head. An advantage of these lasers is the capability for variable pulse repetition frequencies (PRF) accomplished through an acousto-optic q-switching mechanism. For standard operation, the MPL PRF is set to 2.5 kHz. At this rate approximately 20 microjoules per pulse exit the immediate laser aperture. The pulse length is less than 10 ns, and beam divergence at this point is approximately 1.2 mrad, half-angle. The detector is an actively quenched EG&G SPCM-AQ-100 Geiger mode avalanche photodiode (GAPD) photon-counting module. Quantum efficiencies approach 70% with maximum count rates near 20 MHz for these solid-state devices.

The "shared" MPL optical paths coincide through a 20-cm aperture, adjustable focal length, Celestron-made Schmidt-Cassegrain telescope. Early experiments with a coaxial MPL indicated that maintaining a transmit-receive alignment was extremely difficult due to the very small field of view intended. With a common telescope and field-stop, alignment stability is much less of a problem. Also, finding the "boresight" is reduced from a technically challenging operation to the simplicity of sending the transmit pulse to the receiver field-stop. An outline of the initial MPL optical design and a simple raytrace is shown in Fig. 2. With one exception (to be discussed), V1.0 and V2.0 share the same layout.

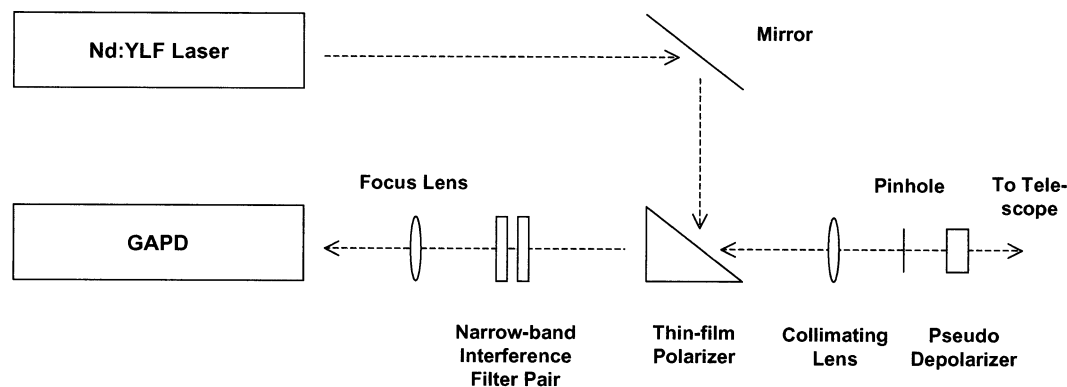


FIG. 2. A simplified 2D outline of the MPL optical design for the V1.0 and V2.0 systems (ARM unit numbers 00, 02, 03, 54, 58, and 59).

Each pulse is turned from the separated laser path to the shared path by a combination angled-mirror and polarizing beam-splitting cube (V1.0) or thin-film polarizer (V2.0). A positive lens then focuses the beam down to the telescope focal point, where a 200- μm pinhole is placed representing the system field-stop (i.e., field-of-view limiting aperture). A pseudorandom depolarizing plate placed beyond the focal point is the last component a pulse interacts with before collimated expansion through the 20-cm-diameter telescope. Ideally, the outgoing pulse divergence is diffraction-limited to approximately 35 μrad . However, inevitable blurring causes the measured value to be more on the order of 50 μrad . Transmission efficiencies through the exit path are on the order of 40%. Outgoing transmitted pulse energies average around 6–8 μJ , which is well within the 25- μJ ANSI eye-safety threshold quoted for a 20-cm-aperture source.

Along the receive path, the telescope focal length is approximately 1.7 m. Given the field-stop diameter, the receiver field of view is approximately 120 μrad . Laboratory measurements demonstrate its effective value to be more on the order of 100 μrad . This extremely narrow field of view eliminates many of the known ambiguities associated with the multiple scattering of the lidar signal (Eloranta 1998) and limits detection of ambient background light. The positive lens behind the pinhole collimates the randomly polarized backscatter, before it passes through the beam-splitter device to the separated receive path. Two narrow interference filters (approximately 1.2- \AA combined spectral width) are placed in front of a final positive lens that focuses energy down onto the detector.

Along the shared portion of the optical axis, an outgoing pulse interacts with four reflective surfaces: the positive lens in front of the pinhole, the outer edges of the pinhole itself, the random depolarizer, and the telescope corrector plate. Backward reflections of the outgoing pulse from these surfaces inadvertently reach the detector. The significance of this energy is enough to momentarily (approximately 200 ns) saturate the GAPD

with the onset of each sampling period. A run-on signal is created by this event, which decays gradually through the length of the sampling period. This so-called afterpulse is of appreciable magnitude, and data postprocessing must account for it. This point will be examined further in section 3b. Laboratory measurements have shown that scatter off of the pinhole contributes significantly to the internal reflections. Therefore, the focus of the detector relative to the pinhole is shifted slightly in the final alignment stages such that the system exit pupil (image of the primary mirror of the telescope) is imaged onto the detector rather than that of the pinhole. However, the size of this image is larger relative to that of the pinhole. It can potentially be larger than the active surface area of the GAPD. In such cases the detector active area is overfilled such that this point becomes the actual system field-stop. The receiver field of view is narrowed slightly in such cases.

An alternate optical configuration can be used to limit the effects of afterpulsing. Such a design decreases the number of reflective surfaces an outgoing pulse interacts with. The pinhole and its corresponding positive/collimating lens are retracted behind the shared path coaxial junction. The pulse still interacts with the telescope corrector plate and random depolarizer, but their contribution to afterpulsing is of much less significance. This design scheme is detailed in Fig. 3. The modification requires an increase in the telescope focal length (approximately 2.0 m) to accommodate the retracted spacing of the pinhole. The receiver field of view lowers to 100 μrad , though laboratory measurements have found the effective value to be approximately 90 μrad . Note that the system focal point must now be set twice, as the outgoing beam no longer interacts with the pinhole. A negative lens is placed just after the turning mirror but before the path junction to accommodate this. A beam-splitting cube is used to turn the beam toward the depolarizer and telescope. The pinhole/positive lens combination rests behind the cube, translating all incoming light to the filters and detector as with the earlier design. As these modifications are logistically rather

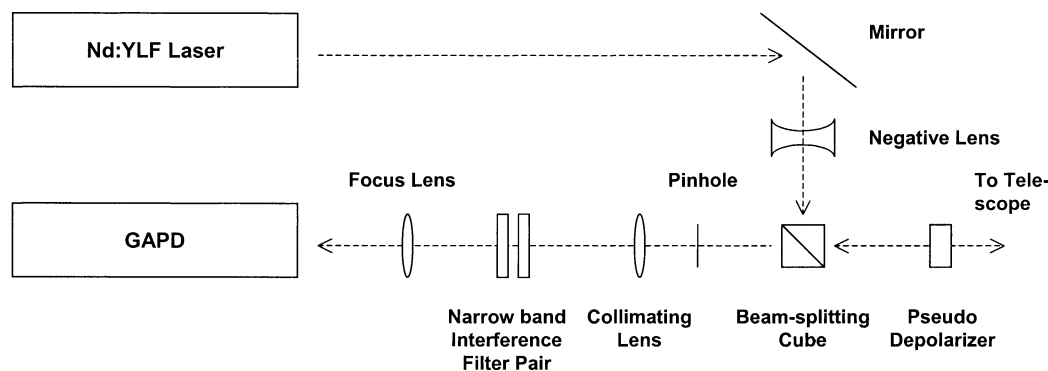


FIG. 3. A simplified 2D outline of the MPL optical design for the V2.1 systems (ARM unit number 72).

simple, V2.0 systems can be upgraded with relatively minor effort. As of March 2001 one ARM unit featured this upgrade (unit 72, which we'll now term V2.1). Additional systems are in the process of being upgraded. A comparison of afterpulsing between a V2.0 and V2.1 system is displayed in Fig. 4; V2.1 modifications significantly lower the effect by roughly an order of magnitude.

The MPL data system consists of a SESI-manufactured multichannel scalar card (MCS) package, connected through a serial cable to the detector. Its output is then read through a National Instruments PC-DIO-24 data-acquisition card and serial cable by a Windows-based software package run by a PC laptop computer. Two versions of the SESI MCS have existed among the ARM units. The earlier version allowed static range sampling periods of $2 \mu\text{s}$ (300-m vertical resolution)

and is no longer used. The current model allows for user-variable settings of 300, 150, 75 and 30 m as regulated through the software interface. ARM systems equipped with this MCS typically use the maximum 30-m-resolution setting. The first three ARM systems (00, 02, and 03) were originally equipped with the low-resolution MCS. The last three (54, 58, 59, and 72) feature the updated model (note that the rather arcane numbering scheme of the systems depends on this feature, as higher-resolution systems simply have a value of 50 added to their original unit number). At a PRF of 2.5 kHz, there is $400 \mu\text{s}$ between consecutive pulses, allowing a range maximum of 60 km of data. A software interface setting allows the user to decide how much of this data is to be saved to the raw output file. This option is important for calculating the amount of ambient background counts persisting during a shot sample, which will be explained further in section 3c. Spinhirne (1993) showed that pulse summation is required to reach appreciable signal-to-noise ratios, given the low outgoing pulse energies. A software setting allows the user to determine the sample-averaging interval by which photon counts per range bin are stored in the data file. ARM systems have historically been set to either 30 or 60 s. The MCS relays temperature readings from three thermistors mounted inside the optics canister. Voltage readings from an energy monitor mounted in front of the laser aperture are transmitted and then converted to microjoules using a lookup table calibrated for each system. Height-sampling period-intensity readings are displayed in real time on the PC screen, along with system diagnostics.

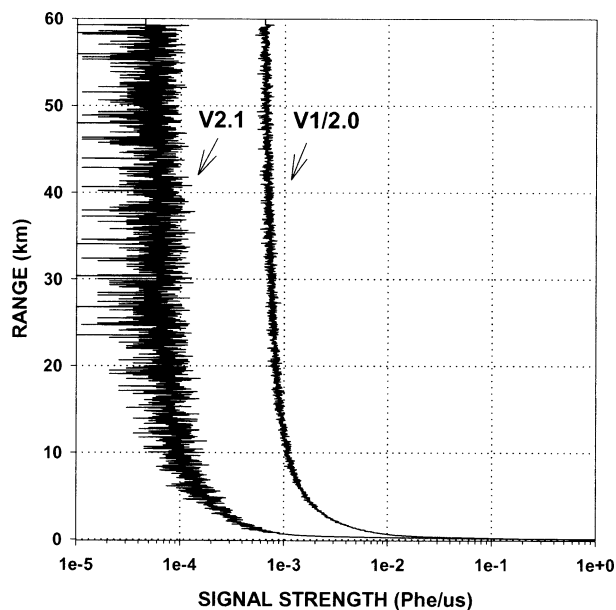


FIG. 4. A comparison of 10-min averaged detector afterpulsing signal profiles (range proportional to time) from original (V1.0 and V2.0) and upgraded retracted pinhole (V2.1) optical configurations in 30-m range resolution.

3. Data processing

Temporally and spatially averaged photon counts (to be referred to simply as "shots") are written to the local storage disk in a simple GSFC-developed binary format concatenated into hourly files. Though software has been developed within the ARM project to simultaneously rewrite these data into the more flexible, and arguably more efficient, netCDF format (C. J. Flynn and B. Ermold 1998, personal communication), we concen-

trate here on the original structure as it pertains to the system software package directly. A header precedes each shot profile, denoting significant system settings (discussed previously) and relevant housekeeping details (e.g., time stamp, energy monitor, component temperatures, etc.) with sum byte size varying by system version. The prototype (unit 00) used a 25-byte header, subsequent low-resolution (LR) MCS systems use 36 bytes, and high-resolution (HR) systems employ 44 bytes. Following the header, shots are broken into range-resolved raw counts via successive four-byte segments taking the form

$$n(r) = \frac{b(1) \cdot 256^3 + b(2) \cdot 256^2 + b(3) \cdot 256 + b(4)}{1.0 \times 10^8} \quad (1)$$

With the effective sampling range set to the maximum 60 km, LR systems can inspect as many as 200 range bins (800 bytes), while HR systems sample a maximum of 2001 bins (8004 bytes). A complete day of LR data using 60-s sample averaging totals nearly 1.2 MB of data, while corresponding HR systems record slightly over 10 times this amount. While interest lies mainly in signal measured (pointed vertically) from the first 20 km, sampling out to the maximum 60 km (as all ARM systems do) serves to measure background counts, which will be discussed below.

At the SGP and NSA sites, raw files are uploaded hourly to central servers. Data recorded at the TWP sites are backed up onto recordable media and delivered to ARM when possible. The ARM Data Center is responsible for data ingest and also manages its storage, dissemination to data users, and postprocessing.

From the lidar equation, MPL raw counts take the form

$$n(r') = \frac{\frac{[O_c(r')CE\beta(r')T(r')^2]}{r'^2} + n_b + n_{ap}(r')}{D[n(r')]} \quad (2)$$

where n equals the measured signal return in photoelectron counts per second at range r' , O_c is the overlap correction as a function of range caused by field-of-view conflicts in the transceiver system, C represents a dimensional system calibration constant, E is the transmitted laser pulse energy, β is the backscatter cross section due to all types of atmospheric scattering, T is atmospheric transmittance, n_b is background contribution from ambient light, n_{ap} is the contribution from afterpulse, and D is the detector photon-coincidence “dead time” factor as a function of raw count rate. Note that range is written in the initial form r' to account for the sum of two offsets (Δr_o) such that

$$r = r' - \Delta r_o, \quad (3)$$

where r is the actual range. The first portion of this offset results from the software recording range being the temporal distance to the end of a sampling bin. To

maintain consistency with other ARM cloud profilers this value is modified to represent the bin center (E. E. Clothiaux and D. D. Turner 1999, personal communication), requiring a subtraction equal to half of the system range resolution. The second portion of the offset accounts for a timing inaccuracy between the laser pulse and MCS triggers. Low-resolution systems have a negative offset such that the laser fires before photon counting begins, while HR systems routinely fire afterward (both vary slightly with system). A simple means of estimating the discrepancy is possible in HR data by examining counts per bin from a representative shot sample (~ 60 s) in 30-m resolution. The first bin where significant counts are present depicts the laser firing, and its range is the spatial offset. This value is routinely on the order of two such range bins, or 60 m (400 ns). Low-resolution systems cannot be calibrated quite as simply because their 300-m maximum resolution is much larger than the standard deviance. However, it has been measured in the laboratory to be roughly -120 m (-800 ns).

After accounting for Eq. (3) in Eq. (2) and moving the various correction terms to the left-hand side, an intermediate value referred to as normalized relative backscatter (NRB) is derived in Eq. (4):

$$\frac{[n(r) \times D[n(r)]] - n_{ap}(r) - n_b}{O_c(r)E} r^2 = C\beta(r)T(r)^2. \quad (4)$$

This value represents the baseline product of ARM value-added processing. Secondary algorithms, including cloud boundary detection and the calculation of significant optical parameters ingest this product as a starting point. Subsequent processing of NRB requires calculation of the system calibration constant (C). Solving for C cannot be done in real time with a single-channel lidar alone. Welton et al. (2001) show that an independent measurement of the vertical column aerosol optical depth offers the most practical means of solving C on a case-by-case basis.

WC02 analyze the uncertainties for each of the correction terms found in (4), as well as a total measure of error in the final NRB signal. The individual terms break down as follows.

a. Dead time $D[n(r)]$

The dead-time correction adjusts for the saturation effect on the GAPD observed at high incident count rates due to the finite width of a single photon avalanche event (PhE). An explicit “dead-time” period associated with recording such an event occurs. Dead time for the EG&G SPCM is specified to be no higher than 60 ns, and actual performances are routinely half this amount. A lookup table is supplied by the manufacturer listing the statistical approximation of the PhE underestimation factor as a function of the component dead time and reported counts per second. The theoretical value of the

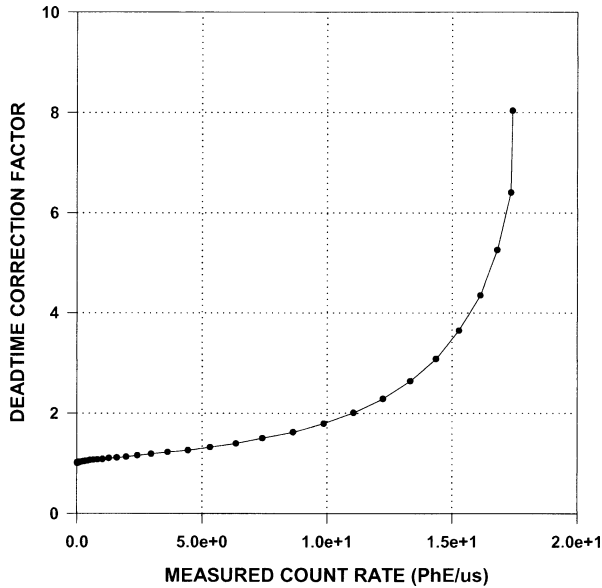


FIG. 5. A sample photon-counting detector dead-time correction. The correction is a function of apparent component-measured photon count rates.

correction factor as specified by the manufacturer follows the equation

$$D[n(r)] = \frac{1}{1 - (\tau_D \times \chi_R)}, \quad (5)$$

where τ_D is the module dead-time value and χ_R is the output count rate (itself a function of the component quantum efficiency). In practice however, the dead-time correction is solved for based on laboratory calibration versus a well-known source. An example relationship is plotted in Fig. 5. Count rates measured with the MPL rarely reach the upper end of the detector resolvable rate spectrum, which is on the order of 10 PhE per microsecond. Detector saturation via atmospheric scatter is very uncommon. Count rates are most frequently measured to be less than 1 PhE per microsecond, which falls within the linear-like region in Fig. 5, or a correction of approximately 1.

b. Afterpulsing ($n_{ap}[r]$)

Afterpulsing is an inadvertent signal by-product caused by the initial laser flash interacting with the GAPD. Internal system reflections saturate the detector diode at the beginning of a sampling period, and a small leakage signal profile is measured for the remaining time period of the shot. (This situation is analogous to that of a human eye staring quickly at a bright object and then blinking, after which brightness can still be sensed for a short period while the eyelid is closed.) Charge dissipation is exponential-like amid the 400- μ s sampling period between laser pulses. Figures 6a and 6c compare averaged profiles of dead time and back-

ground-corrected raw signal where the outgoing pulse was extinguished by a hard target immediately in front of the instrument (discussed further below), versus similar profiles of clear-sky signal, for both the V2.0 and V2.1 instruments, respectively. Figures 6b and 6d show the corresponding percentage contribution to total count rates by afterpulsing for each. It is clear that the contribution of afterpulse can be significant at upper-tropospheric ranges. When processing ARM datasets from the two TWP sites, where cirrus clouds are routinely found near the tropical tropopause to heights approaching 19 km, accurate afterpulse characterization is important (WC02).

Afterpulsing varies among systems as a function of numerous diagnostic variables, including ambient and internal temperatures, transmitted laser pulse energies, and background counts. In practice an empirical relationship cannot be directly derived. Instead, afterpulse calibrations for ARM systems must be done frequently (approximately every month) to maintain accurate data postprocessing. However, the integrity of a single, static correction is jeopardized if the operating stability of the instrument is compromised. Spectra Physics 7300-L3 laser diode output has proven sensitive to continuous fluctuations in the ambient environment temperature. It is intuitive that afterpulsing is a direct function of the energy associated with each transmitted pulse. As such, ARM systems are operated in weather-sealed trailers where typical thermostat settings allow for no more than 2°C ambient variations at most. Internal system temperatures are therefore kept as stable as is generally possible. Also, the afterpulse correction is energy normalized so as to account for unavoidable perturbations in transmitted pulse energies (due to laser aging, dust, etc.). Equation (6) shows this, where $n'_{ap}[r]$ represents the static correction as a function of range, E the shot-average energy monitor reading (μ J), E_0 the average energy monitor reading for the profile used to calculate the correction file, and $n_{ap}[r]$ the final energy-normalized value:

$$n_{ap}[r] = n'_{ap}[r] \times \frac{E}{E_0}. \quad (6)$$

Laboratory measurements have shown this scaling factor to be appropriate.

Isolating afterpulse signal is best accomplished when the system is operated in a “blocked” configuration, where atmospheric backscatter and ambient background counts are eliminated. In such a scenario, signal measured beyond the blocking point (in terms of time) is the sum of detector noise and afterpulse. This can be achieved in a laboratory setting (i.e., a dark room when the system is pointed at a target), or more easily by applying a lid to the transceiver to eliminate background light. Detector noise rates are predetermined and specified by the manufacturer. Subtracting them from a measured profile of count rates at each bin therefore yields

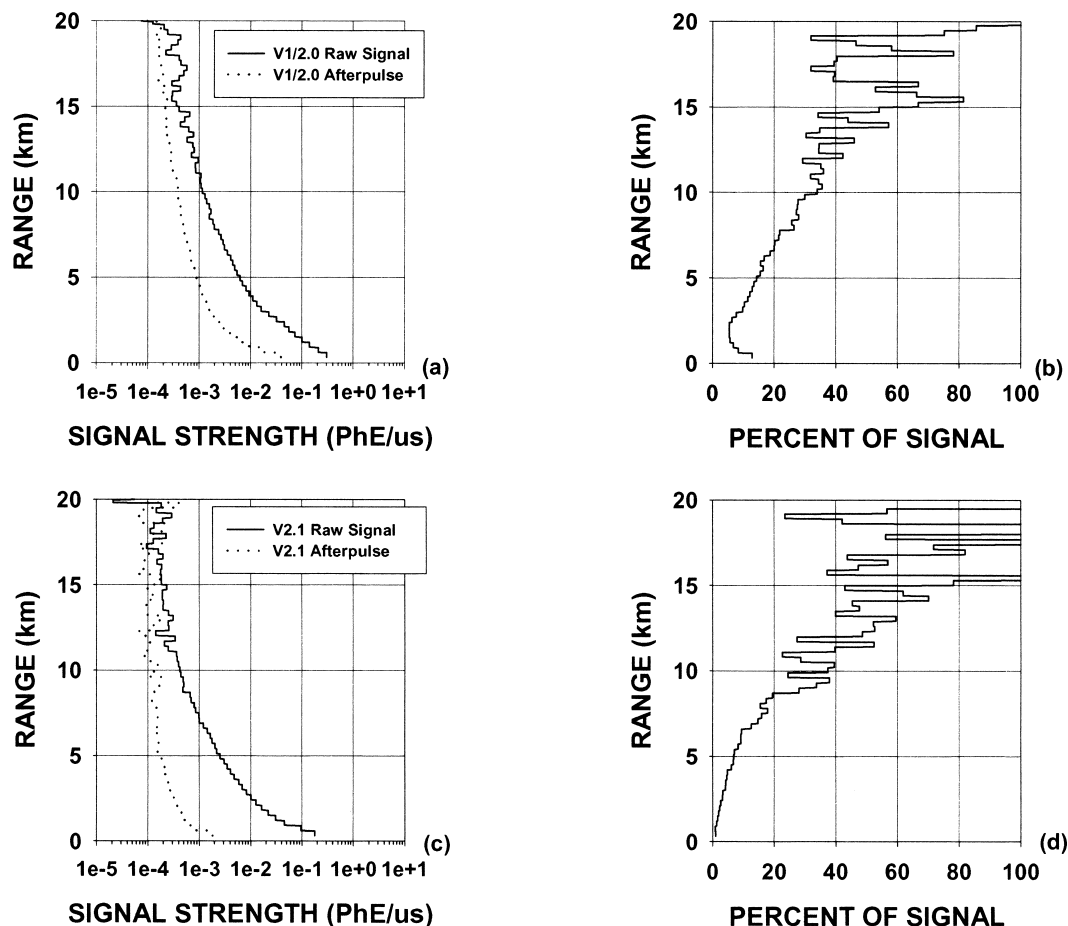


FIG. 6. Comparison of raw photon count rates from total signal and afterpulsing within the troposphere for (a) V1.0 and V2.0 and (c) V2.1 systems, in 300-m range resolution. Relative percentages of afterpulsing to total signal for each are shown in (b) and (d).

afterpulse. It should be noted that detector saturation (discussed earlier) briefly paralyzes the GAPD after each initial laser pulse flash. Raw data collection in the extreme near range is severely compromised by lingering uncertainties in the detector output for as much as $2.0 \mu\text{s}$ (300 m) while the GAPD stabilizes. Processed ARM HR datasets typically do not report data from before this point to avoid potential ambiguity. Low-resolution datasets are somewhat less susceptible to this, due to their lower resolution and additional time offered by the laser/detector trigger offset.

c. Background (n_b)

The narrow MPL receiver field of view greatly limits the amount of ambient background light incident upon the detector; however, its magnitude remains of significance. ARM systems are exclusively operated while pointed vertically, such that beyond ~ 30 km it is presumed that no distinguishable backscatter is measured in the data. What the detector measures from beyond this range is a combination of background, detector

noise, and afterpulsing. The latter value is adjusted first. Any representative sample of bins past 30 km can then be averaged to produce an estimate of the sum of background and dark counts. For ARM postprocessing, bins between 45 and 55 km are used. This limits the effects of potential error in the afterpulse subtraction, since the relative uncertainty in that correction is lowest toward the end of the sampling period (Welton; WC02). The MPL software package performs a similar calculation using bins from 50 to 60 km, storing the value in the shot data header. This particular range is not necessarily the most appropriate, however. Due to the negative laser/MCS offset in LR systems (and potentially HR systems, though none have been seen as of yet), the end of a sampling period would occur after the laser pulse corresponding with the start of the following period, thus contaminating a background measurement. For this reason, the 45–55-km range has historically been used to maintain consistency.

At the low-latitude tropical sites, the MPL is run concurrently with a mechanical shutter mechanism. This apparatus shields the instruments for approximately one

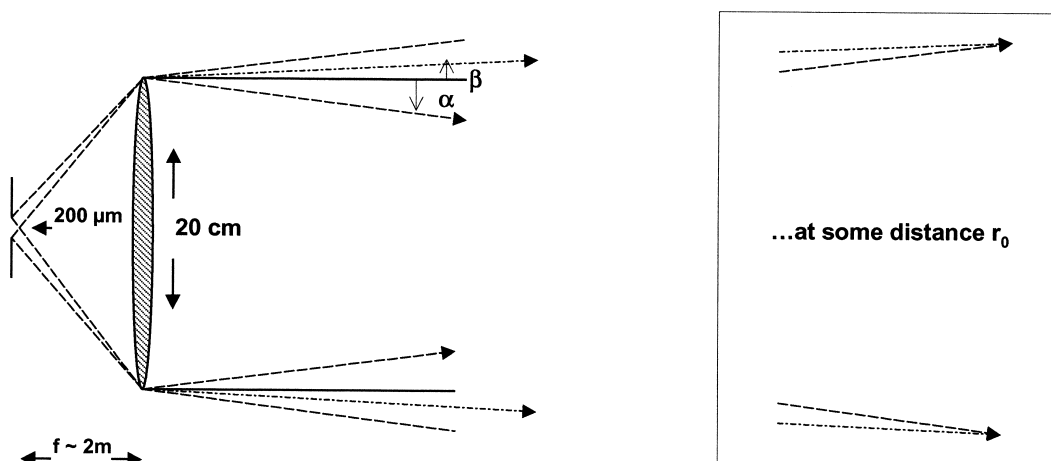


FIG. 7. A simplified 2D sketch of the geometric contribution to overlap in the MPL optical design. Shown is the 200- μm -diameter pinhole and 20-cm-diameter telescope primary mirror. The solid line is the normal to the primary mirror surface. The dashed line represents the field of view (angle α , approx 100 μrad) dictated by the pinhole diameter/telescope focal length combination. The dash-dotted line represents the divergence of the outgoing laser pulse (angle β , approx 50 μrad) after expansion through the Schmidt-Cassegrain telescope. Full overlap occurs at a range (r_0) where opposing edges of the primary can “see” the entire span of the transmitted beam spot. This occurs when the dashed line (field of view) eventually crosses the dash-dotted line (diverging laser pulse) on the opposing side.

hour each day (ceasing data acquisition) when the sun approaches its daily maximum elevation angle. The potential would otherwise exist for GAPD failure from extreme background count-rates as the solar disk nears the instrument field of view.

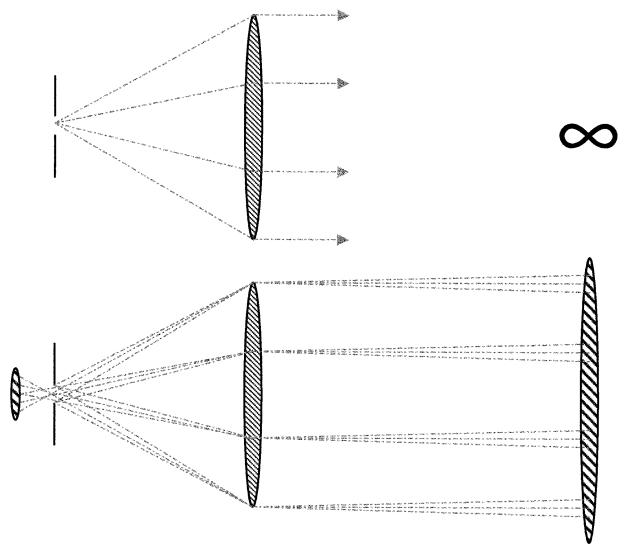


FIG. 8. A simplified, quasi-3D sketch of the optical portion of overlap in the MPL optical design. (top) For an image at infinity, all incident rays are focused down by the telescope to its focal point (i.e., the pinhole). (bottom) Images in the near field focus down behind the pinhole, with a spot-size magnification a function of range and the focal length setting of the Schmidt-Cassegrain telescope. The pinhole however, blocks many of these rays from reaching the image plane, particularly those from outer diverging angles relative to the system field of view. As range increases from the instrument, the image size gradually decreases until the point where vignetting ceases and overlap is reached.

d. Overlap ($O_c[r]$)

The narrow MPL receiver field of view (approximately 100 μrad), combined with the 20-cm transmit/receive aperture (with similarly sized expanded beam-width), creates a near-field signal-vignetting scenario, whereby the near-field optical efficiency of the instrument is compromised. For the shared-transceiver MPL optical design two mechanisms are responsible for “overlap.” Figure 7 illustrates the first aspect by considering opposing points along the ends of a two-dimensional cross section of the MPL telescope primary mirror (the system pupil). Geometrically, factoring in an approximate divergence of the collimated 20-cm outgoing beam ($\sim 50 \mu\text{rad}$), opposing points will not “see” the entire image from a given range until an easily calculable distance (approximately 4.0 km at these settings). It is within this range that the diverging field of view intersects the outer edge of the beam. Optically however, with the field-stop set at the focal point of the transceiver, images in the telescope’s relative near field do not focus down precisely at this point. As a function of range, they focus to a point behind the pinhole with variable image magnification size. This scenario is depicted in Fig. 8. The receiver field of view narrows, and again signal acquisition is compromised in response to vignetting of light from the greater diverging angles by the pinhole. The effects of this optical contribution to overlap linger beyond the geometric point of unity. Typically, V1.0 and V2.0 systems achieve complete overlap just past 5.0 km. The effect in V2.1 systems increases slightly (to approximately 6.0 km) in response to the increased focal length of the telescope and the more narrow field of view.

Measures (1984) offers a detailed treatment of overlap

and develops an equation for calculating the overlap correction as a function of range accounting for both vignetting scenarios. In practice an accurate calculation based on input optical parameters alone is not practical. Overlap is typically solved for experimentally, using a method similar to that described by Sasano et al. (1979). The starting point is an averaged data sample where the system is pointed horizontally with no obscuration. By choosing a time where the atmosphere is well mixed, such as late afternoon, or, even better, when aerosol loading is low, backscatter through the layer is roughly assumed to be constant with range (i.e., the target layer is assumed to be homogeneous). Implicitly, at some range r_o , overlap is complete and the correction factor becomes 1.0. Equation (4) can be written as

$$P(r) = \{(n(r) \times D[n(r)]) - n_b - n_{ap}(r)\} \times \frac{r^2}{E} \\ = O_c(r)C\beta(r)T(r)^2. \quad (7)$$

Knowing that $T(r) = e^{-\tau}$ and $\tau = \sigma r$, where τ is the optical thickness through the layer and σ is the extinction cross section, (7) can be rewritten as

$$P(r) = O_c(r)C\beta(r)e^{-2r\sigma}. \quad (8)$$

For the section of this function where $r > r_o$ and $O_c = 1.0$, taking the natural log of both sides of (8) yields

$$\ln[P(r)] = \ln[C\beta(r)] - 2r\sigma. \quad (9)$$

Since the layer is presumed to be homogeneous, the $\ln[C\beta(r)]$ term is constant. Plotting $\ln[P(r)]$ versus r takes the form of a straight line ($y = mx + b$) past r_o , to the limit of signal attenuation. An example of this is plotted in Fig. 9, where the solid line represents a straight-line fit to the nonlimited region. The extinction term (-2σ) corresponds to the slope (m) of this line, and $C\beta(r)$ is solved for from $\ln^{-1}(b)$ (y -intercept value). These values can then be used to solve for $O_c(r)$ in (8) as

$$O_c(r) = \frac{P(r)}{C\beta(r)e^{-2r\sigma}}. \quad (10)$$

A 4-day concatenated profile of NRB from the TWP-N site for 17–20 January 1999 is displayed in Fig. 10. A very persistent cirrus cloud layer is clearly detected by the instrument through the period, with heights approaching 18.0 km above ground level. The boundary layer is also clearly defined, with varying degrees of aerosol concentration apparent. Intermittent marine stratocumulus cloud cells are mixed in and among the boundary layer. The transmitted beam is attenuated in such cases at very near ranges.

4. Discussion and conclusions

The ARM MPL project is notable for two important achievements. One is the deployment of the first autonomous lidar instruments for full-time operation. Second, the ARM network array provides the first multisite ho-

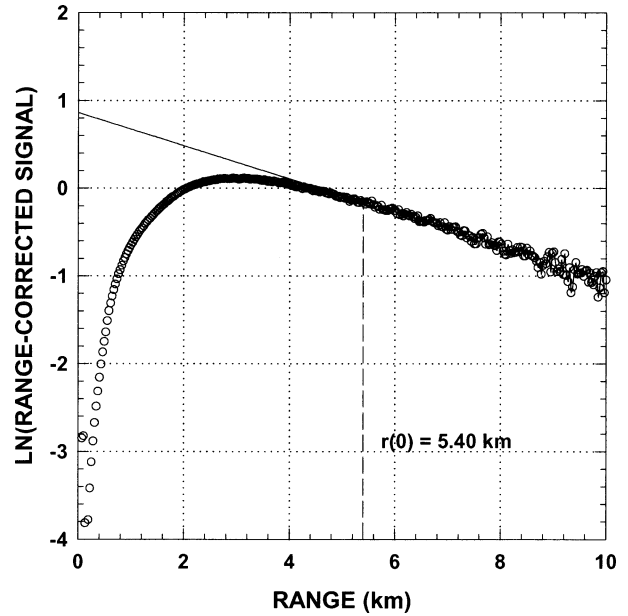


FIG. 9. The natural logarithm of range-corrected, background, dead-time, and afterpulse-corrected MPL data where the system is pointed horizontally. Under well-mixed conditions (i.e., homogeneous target layer) past the point where overlap is achieved, signal falloff is linearly proportional to total incident extinction. In this case, full overlap is reached at approximately 5.40 km.

mogeneous lidar dataset within the community. The practicality of these instruments is derived from eye-safe operation, but low power and compact system size are also important. The MPL features a shared transmit/receive optical path not typically seen in traditional lidar design. Specific conflicts arise through this design. Detector afterpulsing and the near-range overlap function can offer varying degrees of difficulty to data postprocessing if not properly characterized. In this paper, system correction techniques and an algorithm for the normalized relative backscatter (NRB) product are described. Value-added processing of the ARM MPL datastream (available in near-real time and through the ARM archive) is based on these methods. The NRB results are robust when the system correction factors, as described, are properly maintained. Uncertainties in these terms can have various impacts on the final uncertainty associated with NRB (WC02).

MPL instruments have been in operation at ARM sites for over eight years. During that time measures have been taken to insure routine instrument servicing and calibration in the field, as well as the regularly scheduled intensive maintenance only possible in a lab environment. Simple day-to-day maintenance procedures focus on keeping the systems and their immediate environment dust-free. The transmitting window atop the site-operating trailer requires particular attention, because dust and other pollutants from the local surroundings contaminate the window surface, thereby decreasing signal transmission rates. Aside from routine exami-

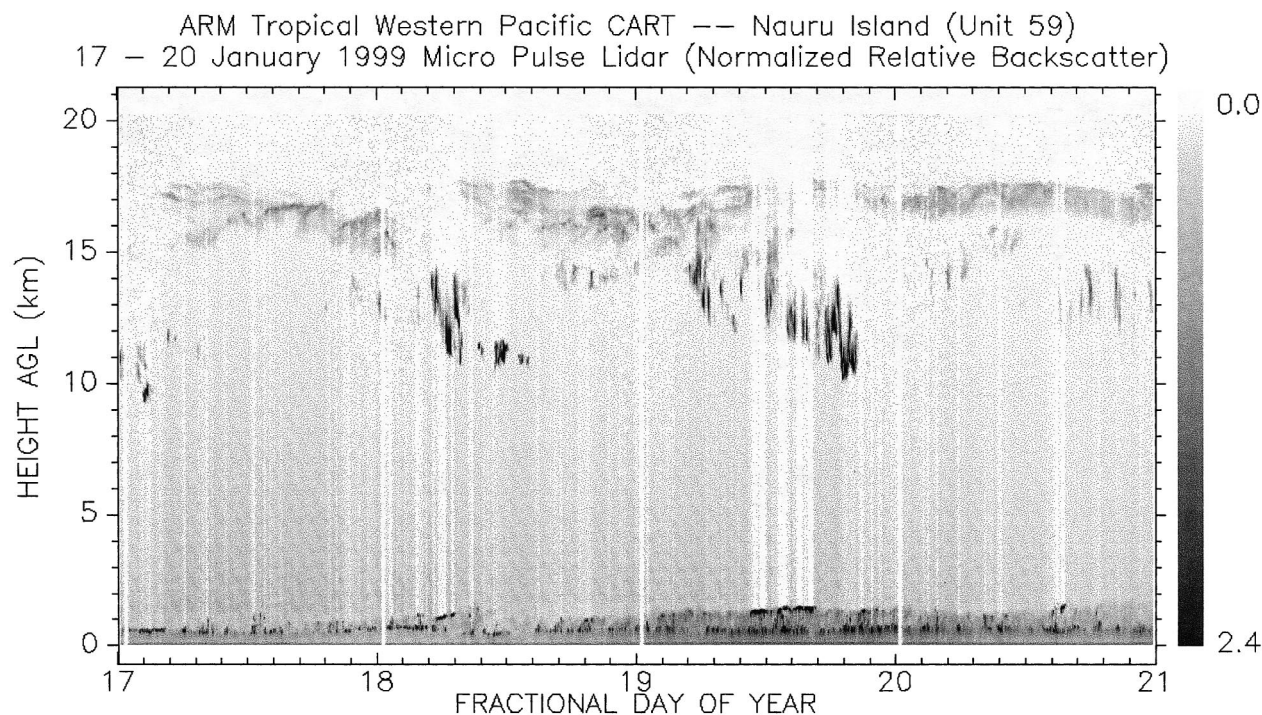


FIG. 10. MPL normalized relative backscatter $\{\text{counts (km}^2) [(\mu\text{J}) (\mu\text{s})]^{-1}\}$ from 17–20 Jan 1999 (fractional days 17–20) collected at the Nauru Island ARM site.

nation of raw data files, ARM instrument mentors can monitor pertinent system diagnostics via the Internet. File and screen sharing software, such as Netopias Timbuktu for Windows, allow for remote manipulation of an MPL system computer. This feature is used with both the SGP and NSA units, where adequate Internet connections exist. Overlap and afterpulse calibrations are monitored during NRB postprocessing. Changes to the optical alignment due to vibration and other aging factors over the period of even a few months are inevitable and must be accounted for. Changes to afterpulsing can be frequent, as the integrity of the system optical path and diode-pumped laser pulse energies are subject to unavoidable fluctuations.

An algorithm by Welton et al. (2001) introduces the next step in the data processing hierarchy, which calculates optical properties for significant atmospheric layers (cloud and aerosol). This routine should be operational within the ARM data-processing fold by winter 2001, providing aerosol extinction cross sections, cloud and aerosol layer optical depths, and planetary boundary layer top heights. Potential data users are encouraged to contact ARM¹ to inquire about specific availability of any such processed datasets. Gaps may exist in some datastreams due to the optical integrity of particular systems during their operation.

Cloud and aerosol studies, both for ARM and poten-

tially similarly motivated global satellite monitoring programs, benefit from extended MPL observations. The vertical distribution of atmospheric constituents is an indirect and ambiguous measurement for passive remote sensors. The application of direct, autonomous lidar systems, as a complement to a collocated suite of passive sensors, brings forth a nearly complete vertical characterization of the radiative state of the atmosphere. The ARM MPL project has demonstrated the practicality of small, continuous running lidars included among intensive remote sensing instrumentation arrays. The need to bring about routine lidar application, onto scales similar to its analogous counterpart radar, is evidenced by the emphasis on cirrus clouds and aerosols as important radiative modulators (e.g., Liou 1986; Schwartz et al. 1995). Sassen and Campbell (2001) assembled 2200 h of ruby lidar observations taken over a 10-yr period to construct a midlatitude cirrus cloud climatology at Salt Lake City, Utah. This represents one of the more definitive such studies so far produced. In comparison, ARM MPL instruments compile 2200 h of data in just over three months. Similarly, Turner et al. (2001) have computed seasonal mean aerosol extinction profiles over the SGP site from 2 yr of Raman lidar data. However, large Raman lidar systems are too expensive to be practically considered for networklike deployment. These comparisons demonstrate the abundant possibility for routine MPL observations. As upgrades and modifications are made to the technology, particularly with regards to implementing dual-wavelength

¹ Information regarding the ARM program can be found online at <http://www.arm.gov/>.

and polarization-scattering capabilities, the potential offered by MPL systems is substantial.

Acknowledgments. MPL research at NASA GSFC has been funded by DOE Interagency Agreement DE-AI01-92ER61367 as part of the ARM program, and through the NASA Radiation Sciences program. Battelle Memorial Institute for the U.S. Department of Energy under Contract DE-AC06-76RLO 1830 operates Pacific Northwest National Laboratory. The authors thank M. McGill of NASA GSFC for many valuable discussions and input, and R. Perez (PNNL) for assistance overseeing the production and archiving of the ARM MPL data archive. We also gratefully acknowledge the comments and suggestions of two anonymous reviewers in significantly enhancing the original version of this manuscript.

REFERENCES

- Eloranta, E. W., 1998: Practical model for the calculation of multiply scattered lidar returns. *Appl. Opt.*, **37**, 2464–2472.
- Liou, K.-N., 1986: Influence of cirrus clouds on weather and climate processes: A global perspective. *Mon. Wea. Rev.*, **114**, 1167–1199.
- Measures, R. M., 1984: *Laser Remote Sensing: Fundamentals and Applications*. Wiley, 510 pp.
- Sasano, Y., H. Shimizu, N. Takeuchi, and M. Okuda, 1979: Geometrical form factor in the laser radar equation: An experimental determination. *Appl. Opt.*, **18**, 3908–3910.
- Sassen, K., 1991: The polarization lidar technique for cloud research: A review and current assessment. *Bull. Amer. Meteor. Soc.*, **72**, 1848–1866.
- , 1995: Lidar cloud research. *Rev. Laser Eng.*, **23**, 148–153.
- , and J. R. Campbell, 2001: A remote sensing midlatitude cirrus cloud climatology from the Facility for Atmospheric Remote Sensing. Part I: Macrophysical and synoptic properties. *J. Atmos. Sci.*, **58**, 481–496.
- Schwartz, S. E., and Coauthors, 1995: Group report: Connections between aerosol properties and forcing of climate. *Aerosol Forcing of Climate*, R. J. Charlson and J. Heintzenberg, Eds., John Wiley and Sons, 251–280.
- Spinhrne, J. D., 1993: Micro pulse lidar. *IEEE Trans. Geosci. Remote Sens.*, **31**, 48–55.
- , J. A. R. Rall, and V. S. Scott, 1995: Compact eye safe lidar systems. *Rev. Laser Eng.*, **23**, 112–118.
- Stokes, G. M., and S. E. Schwartz, 1994: The Atmospheric Radiation Measurement (ARM) Program: Programmatic background and design of the cloud and radiation testbed. *Bull. Amer. Meteor. Soc.*, **75**, 1201–1221.
- Turner, D. D., R. A. Ferrare, and L. A. Brasseur, 2001: Average aerosol extinction and water vapor profiles over the southern Great Plains. *Geophys. Res. Lett.*, **28**, 4441–4444.
- Welton, E. J., and Coauthors, 2001: Measurements of aerosol vertical profiles and optical properties during INDOEX 1999 using micro-pulse lidars. *J. Geophys. Res.*, in press.
- Wielicki, B. A., R. D. Cess, M. D. King, D. A. Randall, and E. F. Harrison, 1995: Mission to planet Earth: Role of clouds and radiation in climate. *Bull. Amer. Meteor. Soc.*, **76**, 2125–2153.